Journal of Inorganic and General Chemistry
ZAAC
Zeitschrift für anorganische und allgemeine Chemie
www.zaac.wiley-vch.de
RESEARCH ARTICLE

DOI: 10.1002/zaac.202200227

Influence of the Cation on the Reaction Mechanism of Sodium Uptake and Release in Bivalent Transition Metal Thiophosphate Anodes: A Case Study of $Fe_2P_2S_6$

Jonas van Dinter,[a] Sylvio Indris,[b] Martin Etter,[c] Giannantonio Cibin,[d] and Wolfgang Bensch*[a]

Dedicated to Prof. Dr. Wolfgang Schnick on the Occasion of his 65th Birthday.

The layered active material $Fe_2P_2S_6$ was examined as anode material in sodium-ion batteries (SIBs) and compared to previously investigated $Ni_2P_2S_6$. A reversible specific capacity of 540 mAh g^{-1} was achieved after 250 cycles, depicting similar electrochemical performance as observed for $Ni_2P_2S_6$. The rate capability and long-term behavior of these two materials are also very similar. Another objective was to elucidate the reaction mechanism during discharging and charging by applying several techniques such as X-ray diffraction, pair distribution function analysis as well as X-ray absorption and solid state NMR spectroscopy. The results clearly demonstrate that the majority of Fe^{2+} is reduced to elemental Fe during the uptake of 5 Na/f.u., while an amorphous intermediate is generated, which was identified as $Na_4P_2S_6$ by solid state NMR spectroscopy. Completely discharging against a Na metal counter electrode leads to the formation of nanocrystalline Na_2S and indications of the formation of polymeric phosphorus were found. In sum, the Na uptake reaction process observed for $Fe_2P_2S_6$ coincides with the previously unraveled reaction pathway of $Ni_2P_2S_6$. We therefore conclude that a universal reaction takes places for bivalent transition metal thiophosphate ($M_2P_2S_6$) electrodes in SIBs.

Introduction

Rechargeable batteries have become a more and more important part of everyday life over the last decades. Whether in the form of the long-known lead acid battery or the dominant and market-leading lithium-ion battery (LIB) for mobile devices, those technologies are an integral element of modern life by now. Especially in light of the imminent climate crisis and the continuous progression of renewable power plants, requirements concerning rechargeable large-scale batteries are rising steadily. Therefore and because of availability, price and sustainability contemplations, the application of sodium-ion batteries often is recommended.[1–6] The biggest advantages are the high abundance and hence low cost of sodium compared to lithium,[1,5,6] while the issue of the larger atomic mass is not as severe as often stated. Particularly for stationary applications, where the weight and footprint of devices are less important, the utilization of SIBs is worth considering.[7,8] While the cathodes for SIBs are often similar to those used in LIBs,[4–10] graphite anodes deliver inherently low specific capacities against Na.[1,11] For that reason, the identification of suitable anodes for SIBs, providing high energy densities and long-term performance while consisting of earth-abundant, low-cost and sustainable elements, has been one of the primary topics in recent SIB-related research.

While a plethora of electrode materials for SIBs has been studied to date (such as carbonaceous compounds,[12–14] various metal chalcogenides,[15–19] alloy-based materials[19–21] amongst others[2,19,21–23]), only few substance classes remain underexplored. One of those less studied material classes is the thiophosphate family. Therefore, we have evaluated different transition metal thiophosphates (MTPs) as anodes in SIBs in the last few years and have shown that some MTPs deliver appropriate electrochemical performances. Moreover, another objective of these studies was the understanding of the occurring reaction mechanisms. Shortly summarizing, we were able to demonstrate that the anodes $Ni_2P_2S_6$, $CrPS_4$ and $CuCrP_2S_6$ each follow individual reaction pathways instead of a universal mechanism (see Eq. (1)–(3)).[24–26] While this might be unexpected at first, these results are quite sound when considered carefully. Each of the compounds can be categorized into different kinds of MTPs, namely into M^{II} ($M_2P_2S_6$), M^{III}

---

[a] J. van Dinter, W. Bensch
Institute of Inorganic Chemistry, Kiel University, Max-Eyth-Str. 2, 24118 Kiel, Germany
E-mail: wbensch@ac.uni-kiel.de
[b] S. Indris
Institute for Applied Materials - Energy Storage Systems, Karlsruhe Institute of Technology, P.O. Box 3640, 76021 Karlsruhe, Germany
[c] M. Etter
Deutsches Elektronen-Synchrotron (DESY), Notkestr. 85, 22607 Hamburg, Germany
[d] G. Cibin
Diamond Light Source, Harwell Science and Innovation Campus, Diamond House, Didcot, Oxfordshire OX11 0DE, United Kingdom

Supporting information for this article is available on the WWW under https://doi.org/10.1002/zaac.202200227

(MPS_4) and mixed M^IM^{III} ($MM'P_2S_6$) thiophosphates, giving rise to different mechanisms according to the equations 1–3.

$$\mathrm{Ni_2P_2S_6} \xrightarrow{+4\ \mathrm{Na}} \mathrm{Na_4P_2S_6} + 2\ \mathrm{Ni} \xrightarrow{+8\ \mathrm{Na}} 2\ \mathrm{Ni} + 6\ \mathrm{Na_2S} + 2\ \mathrm{P} \tag{1}$$

$$\mathrm{CrPS_4} \xrightarrow{+2\ \mathrm{Na}} \mathrm{Na_xCrPS_4} + \mathrm{Na_yCrPS_4} \xrightarrow{+6\ \mathrm{Na}} \mathrm{Cr} + 4\ \mathrm{Na_2S} + \mathrm{P} \tag{2}$$

with ($x + y = 2\ \&\ x \neq y$).

$$\mathrm{CuCrP_2S_6} \xrightarrow{+2\ \mathrm{Na}} \mathrm{Na_2Cu_{1-x}CrP_2S_6} + x\ \mathrm{Cu} \xrightarrow{+10\ \mathrm{Na}} \mathrm{Cu} + \mathrm{Cr} + 6\ \mathrm{Na_2S} + 2\ \mathrm{P} \tag{3}$$

It is noteworthy that the state of phosphorus in the discharged electrodes is still unknown. Most certainly no atomic phosphorus (but likely some sort of P^0; *e.g.* polymeric P) is formed, which is why these reactions should be viewed as formal equations.[24–26]

Although all of the studied MTPs follow individual reaction mechanisms, it is very likely that anodes of the same category, *e.g.* M^{II}TPs, $M_2P_2S_6$, indeed react according to a universal mechanism. Hence, we focused the research on this assumption and studied $Fe_2P_2S_6$ anodes. If the assumption is correct, a reaction involving 12 Na per formula unit (f.u.) would apply according to Eq. (4) and the specific capacity amounts to 879 $\mathrm{mAh\,g^{-1}}$.

$$\mathrm{Fe_2P_2S_6} \xrightarrow{+4\ \mathrm{Na}} \mathrm{Na_4P_2S_6} + 2\ \mathrm{Fe} \xrightarrow{+8\ \mathrm{Na}} 2\ \mathrm{Fe} + 6\ \mathrm{Na_2S} + 2\ \mathrm{P} \tag{4}$$

Besides studying structural and electronic changes during the discharge and charge process, another highly interesting question was how $Fe_2P_2S_6$ performs electrochemically compared to its Ni analogue. While the electrochemical characterization of this anode material was carried out using standard methods, previous studies on the reaction mechanisms of different anode materials have shown that the structural characterization of the ongoing reaction mechanisms usually requires multiple complementary techniques.[24,25,27–30] Accordingly, the reaction mechanism of sodium uptake and release in $Fe_2P_2S_6$ anodes was examined extensively and in a similar way as previously done for $Ni_2P_2S_6$[24] using X-ray diffraction (XRD), X-ray absorption spectroscopy (XAS), pair-distribution function (PDF) analysis as well as $^{31}P/^{23}Na$ magic-angle-spinning (MAS) nuclear magnetic resonance (NMR) spectroscopy.

Results and Discussion

Characterization of Pristine $Fe_2P_2S_6$

$Fe_2P_2S_6$ crystallizes, like $Ni_2P_2S_6$, in the monoclinic space group *C2/m* with similar lattice parameters of $a = 5.947$ Å, $b = 10.300$ Å, $c = 6.722$ Å, $\beta = 107.16°$ and $V = 393.43$ Å^3.[31] The XRD pattern (Figure 1) demonstrates that phase pure $Fe_2P_2S_6$ was obtained. However, some less intense expected Bragg reflections are absent and intensity ratios are slightly different than expected. Possible reasons are structural defects, such as stacking faults, rotational disorder or texture induced by shear forces during grinding. Especially the layered MTPs are prone to these kinds of defects. The potential occurrence of those defects has been discussed already elsewhere in more detail.[32–35] Besides, previous investigations on the structure of $Ni_2P_2S_6$ revealed hexagonal distortions of the monoclinic symmetry,[24] which potentially cause or at least contribute to the observed phenomenon as well.

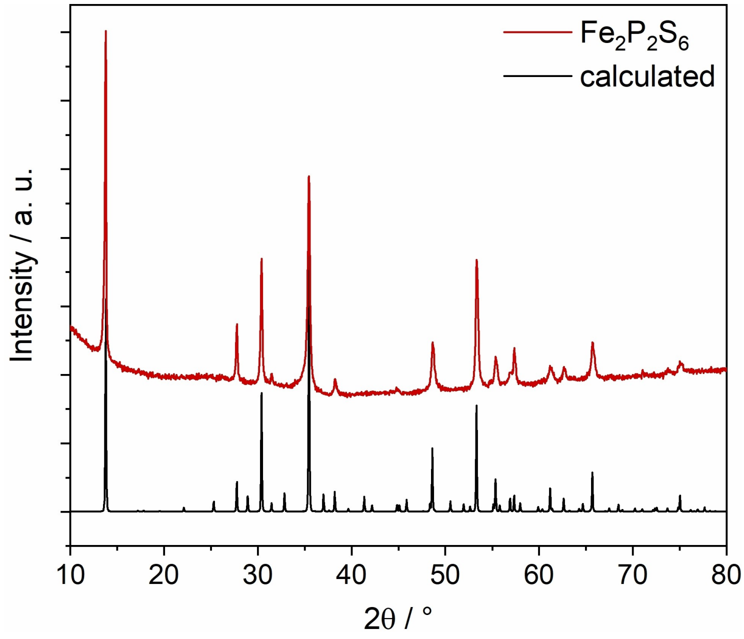

Figure 1. XRD pattern of $Fe_2P_2S_6$ compared to a pattern calculated from literature data.[31] The XRD pattern was collected using Cu-K_α radiation ($\lambda = 1.54058$ Å).

Combined EDX and elemental analysis (Table S1 & S2) yield the composition $Fe_{1.97}P_{1.98}S_{6.05}$ in very good agreement with the expected stoichiometry of $Fe_2P_2S_6$. Additional SEM images confirm the layered structure of the compound (Figure S1).

Electrochemical Performance

Here, the electrochemical long-term performance of $Fe_2P_2S_6$ electrodes (Figure 2a) is compared to values previously reported for $Ni_2P_2S_6$ electrodes.[24] In the first cycle, $Fe_2P_2S_6$ electrodes deliver an initial discharge capacity of 1181 mAh g^{-1} (~16.1 Na/f.u.), while the initial charge capacity amounts to 854 mAh g^{-1} (~11.7 Na/f.u.). The Coulombic efficiency is nearly 100% from the 3rd cycle onwards. Within the first 15 cycles, the specific capacity reaches a minimum of 478 mAh g^{-1} (~6.5 Na/f.u.) and thereafter increases continuously to 638 mAh g^{-1} (~8.7 Na/f.u.) in the 144th cycle. Subsequently, the capacity slowly decreases until 540 mAh g^{-1} (~7.4 Na/f.u.) are obtained after 250 cycles. In the 190th cycle (maximum cycle number reported for bulk $Ni_2P_2S_6$), $Fe_2P_2S_6$ delivers a specific capacity of 614 mAh g^{-1} (~8.4 Na/f.u.), which is almost identical to the value obtained for $Ni_2P_2S_6$ electrodes (621 mAh g^{-1}; ~8.6 Na/f.u.).[24] Moreover, the shapes of the discharge/charge profiles (Figure 2b; *cf.* ref. [24]) of these two materials are similar, exhibiting pronounced potential plateaus in the discharge step at 1.4–1.5 V as well as less pronounced pseudo-plateaus during charging between 1.7 V and 1.9 V. Especially the well-pronounced potential plateau in the discharge process is a typical sign for an intercalation reaction, while the shape of the discharge curve after this plateau indicates a common conversion reaction. The charge process most likely proceeds via conversion, which is indicated by the indistinct course of the charge curve and the aforementioned less pronounced pseudo-plateau. Therefore, the discharge and charge profiles of $Fe_2P_2S_6$ electrodes suggest similar reaction steps during Na uptake and release as previously observed for $Ni_2P_2S_6$.[24] Further comparison with $Ni_2P_2S_6$ electrodes reveal several other similarities: $Fe_2P_2S_6$ and $Ni_2P_2S_6$ electrodes exhibit a pronounced discrepancy between the first discharge and charge capacity, and for both materials,

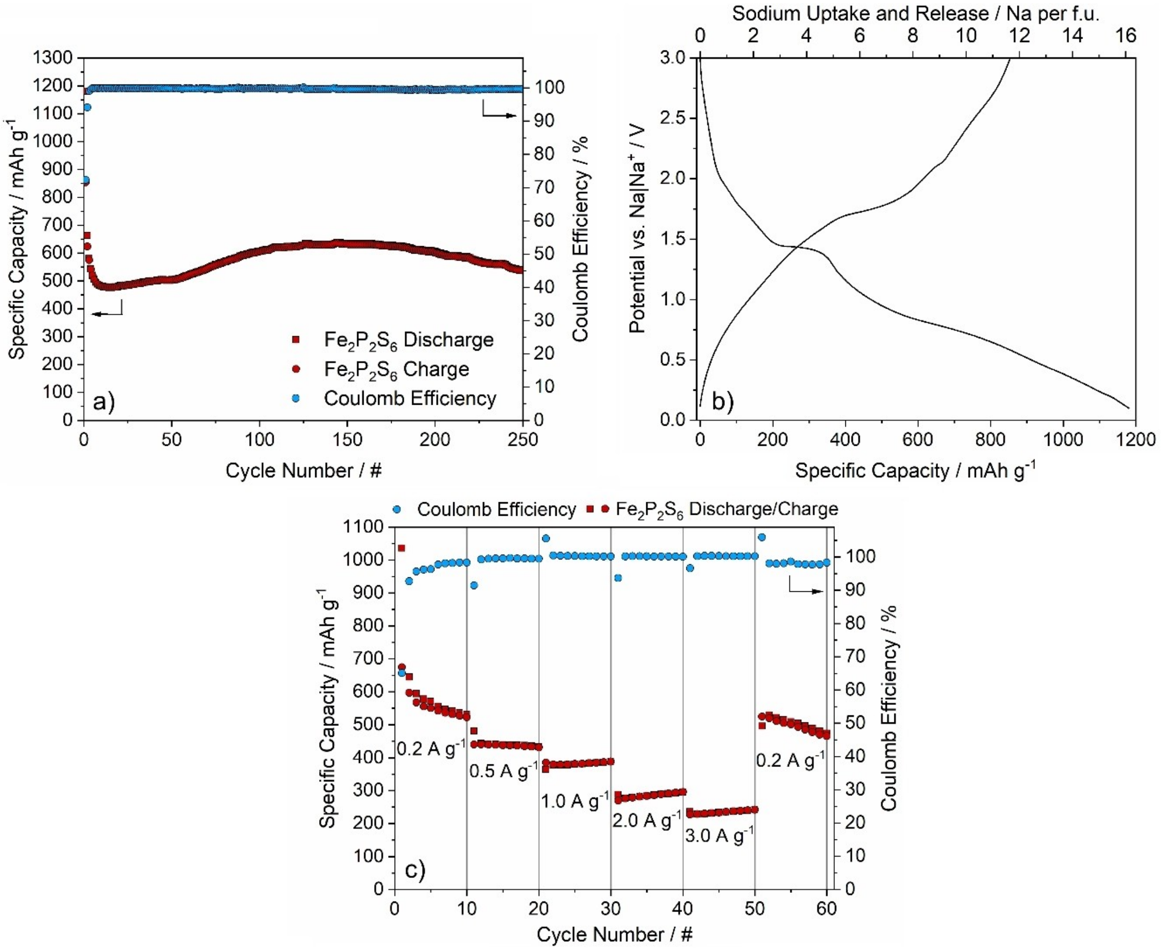

Figure 2. (a) Electrochemical long-term performance, stability and Coulomb efficiency of $Fe_2P_2S_6$ electrodes vs. Na metal. A current rate of 1 A g^{-1} was applied and the electrode was cycled within a potential range between 3.0 and 0.1 V. (b) Discharge/charge curve of the initial cycle of $Fe_2P_2S_6$ electrodes vs. Na metal. (c) Rate capability measurement with current densities ranging between 0.2 and 3.0 A g^{-1} in the same potential window.

a capacity fading within the early cycles is clearly evident. While the initial irreversible capacity (difference between the initial discharge and charge capacity) is larger for $Fe_2P_2S_6$ (~4.4 Na/f.u.) compared to $Ni_2P_2S_6$ (~2.3 Na/f.u.),[24] the initial charge capacity of the two electrodes is very similar, i.e. the same amount of Na/f.u. is released in the first charge process (~11.7 Na/f.u. in both cases). The observed capacity fading within the early cycles is less pronounced for $Fe_2P_2S_6$ and occurs over a smaller number of cycles than for $Ni_2P_2S_6$.[24] Both materials experience a capacity increase after the initial capacity fading. While such observations can have several reasons,[24,25,36–38] it is most likely that a changing electrochemical reaction during long periods of cycling is responsible in this case. The successive changing of discharge/charge profiles (see ESI; Figure S2) during extended cycling is an obvious indication of a changing long-term mechanism, which is a common observation for MTP compounds[24–26] as well as for other conversion electrodes.[27–29,36,38,39]

For further electrochemical characterization, rate capability experiments (Figure 2c) were conducted applying increasing current rates (0.2, 0.5, 1.0, 2.0, 3.0 and again 0.2 $A\,g^{-1}$) for 10 cycles each. Increasing the current rate from 0.2 to 3.0 $A\,g^{-1}$ results in decreased specific capacities in the 10th cycle (Table 1). It shows that the electrochemical rate stability of $Fe_2P_2S_6$ and $Ni_2P_2S_6$ is very similar. However, it is noteworthy that $Ni_2P_2S_6$ appears to be slightly more tolerant against high currents ($\geq$ 2.0 $A\,g^{-1}$), while $Fe_2P_2S_6$ exhibits a better capacity retention when switching back to low currents.

In sum, the electrochemical behavior of $Fe_2P_2S_6$ and $Ni_2P_2S_6$ electrodes is very similar, which is not surprising due to their strong similarities in structure and composition. Despite the observed similarities, some differences were observed as well, which manifest in the slightly faster recovery of the capacity during long-term cycling for $Fe_2P_2S_6$ and the larger tolerance against high currents for $Ni_2P_2S_6$. However, these differences are rather small compared to the similarities. Moreover, the electrochemical performance of $Fe_2P_2S_6$ is comparable to other MTP electrodes (Table 2).

It is further noteworthy that the obtained values for $Fe_2P_2S_6$ depict an appropriate overall performance for conversion electrodes as well. However, in contrast to many other high-performance electrode materials, which usually contain toxic Ni or Co, $Fe_2P_2S_6$ only contains nontoxic Fe as redox active metal making it a relatively safe active material for SIBs with promising electrochemical properties.

Table 1. Results of rate capability experiments for the $Fe_2P_2S_6$ electrode compared with previously reported values for $Ni_2P_2S_6$.

Electrode Current Rate [$A\,g^{-1}$]	$Fe_2P_2S_6$ Capacity[a] [$mAh\,g^{-1}$]	Retention[b] [%]	$Ni_2P_2S_6$[24] Capacity [$mAh\,g^{-1}$]	Retention [%]
0.2	531	100	739/792[c]	100
0.5	433	82	622	84/79[c]
1.0	387	73	558	76/70[c]
2.0	295	56	488	66/62[c]
3.0	241	45	392	53/50[c]
0.2	474	89	588	80/74[c]

[a] Specific capacity after 10 cycles of the applied current rate. [b] In relation to the capacity obtained for the lowest current rate in the 10th cycle. [c] For the sake of proper interpretation of the obtained values, an averaged specific capacity of 792 $mAh\,g^{-1}$ was used in Ref. [24] for the current rate of 0.2 $A\,g^{-1}$ due to steadily decreasing capacities for this rate. Here, this averaged value as well as the value in the 10th cycle were used for the comparison with $Fe_2P_2S_6$ electrodes.

Table 2. Comparison between the long-term stability and rate capability of different MTP compounds. The operating potential range was equal for all compounds (0.1–3.0 V) and the electrodes were made from bulk material in every case.

anode material	long-term stability capacity/current/cycles [$mAh\,g^{-1}$]/[$mA\,g^{-1}$]/[#]	rate capability[a] capacity/current/retention [$mAh\,g^{-1}$]/[$mA\,g^{-1}$]/[%]	reference
$Fe_2P_2S_6$	540/1000/250	433/500/82 241/3000/45	This work
$Ni_2P_2S_6$	621/1000/190	622/500/84 392/3000/53	[24]
$CrPS_4$	687/1000/300	422/500/76 288/3000/52	[25]
$CuCrP_2S_6$	409/1000/200	566/500/66 422/3000/49	[26]

[a] rate capabilities with current rates of 0.5 and 3.0 $A\,g^{-1}$ are shown. The values of the capacities were obtained after completion of 10 cycles with the indicated current rate.

Investigations of the Reaction Mechanism of the Initial Cycle

In order to gather enough material required for the investigation of the reaction pathway of the 1st cycle, pressed powder electrodes instead of film electrodes were produced. Similar to observations made for $Ni_2P_2S_6$,[24] powder electrodes of $Fe_2P_2S_6$ (Figure S3) yield a lower initial specific capacity (948 mAh g^{-1} ≈ 12.9 Na/f.u.) compared to film electrodes (1181 mAh g^{-1} ≈ 16.1 Na/f.u.). Nonetheless, the specific discharge capacity of powder electrodes matches the theoretical capacity of 879 mAh g^{-1} (12 Na/f.u.) very well. The discrepancy between the specific discharge capacities of $Fe_2P_2S_6$ film and powder electrodes also mirrors the observations made for $Ni_2P_2S_6$ (film vs. powder electrodes: 14.0 vs. 12.1 Na/f.u.).[24] The reason for this is most likely the larger electrode loading (powder vs. film: 29.68 mg cm^{-2} vs. 1.16 mg cm^{-2}) causing Na^+ transport limitations. Another contribution to the enhanced initial discharge capacity of film electrodes might be co-intercalation of solvent molecules into the layered electrode. For the recharge process, the usage of powder electrodes was not successful, and therefore film electrodes with a larger surface area (Ø = 25 mm) were used in order to obtain sufficient recoverable active material (see ESI for details on powder vs. film cells and the corresponding discharge/charge profiles; Figure S3).

In the subsequent sections of this article, the electrochemical reaction of the initial cycle of $Fe_2P_2S_6$ is explained in detail using results from XRD, PDF, XAS and MAS NMR techniques. Additionally, the findings are compared to the initial cycle of $Ni_2P_2S_6$ in order to answer the question if and to what extent the reaction mechanisms of these two related compounds coincide.

X-Ray Diffraction Experiments

In general, the XRD patterns of the sodiated samples (Figure 3) clearly indicate a steadily decreasing crystallinity of $Fe_2P_2S_6$ with increasing Na uptake. Starting from the pristine material, discharging immediately (+0.5–1 Na/f.u.) results in the appearance of a new intense reflection at 1.61 °2θ (d = 7.33 Å). Some smaller alterations occur at 2.20–3.30, 3.94, 4.19, 4.52 and 6.79 °2θ in the form of new reflections or development of shoulders. Especially the occurrence of the intense reflection at 1.61 °2θ is indicative for an intercalation process. However, the corresponding *d*-value exhibits no integer relation to any other reflection and hence is most likely related to staging phenomena, whereby Na^+ is arbitrarily intercalated into the layers of $Fe_2P_2S_6$ causing only a single additional (00*l*) reflection, which represents the average expansion of the interlayer space. The observed minor changes indicate ongoing structural alterations and most likely are consequences of the arbitrary intercalation of Na^+ into the layers as well (*e.g.* enhanced intensity of (200) reflection at ~4.19 °2θ due to the scattering power of Na within the van der Waals gaps). However, it is not possible to ascribe these reflections to a certain compound due to the smeared intensity and the decreasing crystallinity of the corresponding phase upon Na uptake. After the uptake of 4 Na/f.u. none of these low intensity reflections is visible anymore, and the most

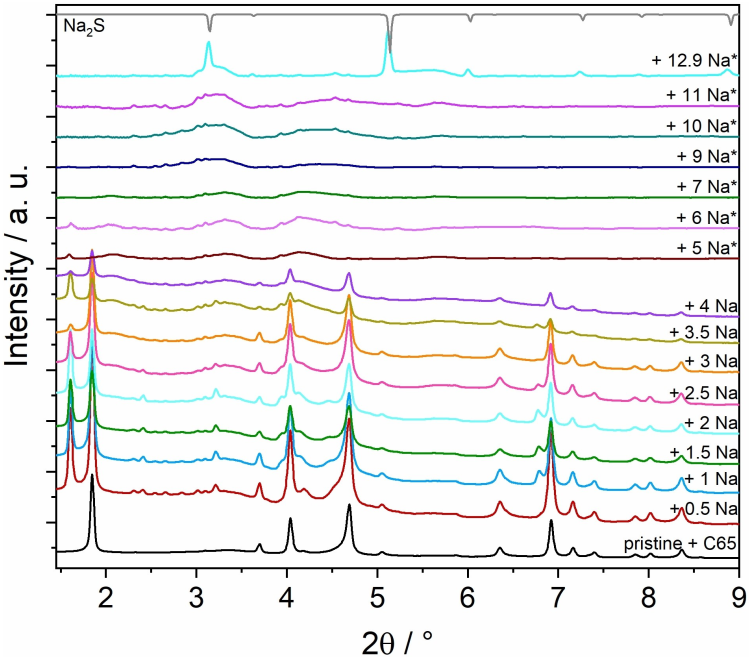

Figure 3. XRD patterns of $Fe_2P_2S_6$ electrodes at different states of discharge. The pattern of Na_2S was calculated from literature data.[40] The XRD patterns were collected using synchrotron radiation with a wavelength of λ = 0.207 Å. Patterns marked with an * were collected at a different beam time period.

intense reflection related to the intercalation at 1.61 °2θ nearly disappeared. At this state, some of the intense reflections of the starting material are still visible. Increasing the Na content further leads to the disappearing of those reflections, i.e. the complete loss of long-range order. Thus, after the uptake of 5 Na/f.u., only broad areas of slightly increased intensity (2.8–3.6 °2θ; 3.8–4.8 °2θ) are observable demonstrating the presence of amorphous or nanocrystalline phases. The only exception is the area between 2.2 and 3.3 °2θ, which shows some low intensity reflections that do not change much during the discharge process and most likely belong to residues of the electrolyte salt, which has been observed already.[27,30] Further Na uptake results in the formation of Na_2S in the completely discharged state. In the recharged state (Figure S4), only NaF is identified unambiguously, which is caused by the formation of a solid electrolyte interphase (SEI).

It is noteworthy that an almost identical behavior has been observed for $Ni_2P_2S_6$ electrodes.[24] Consequently, at least similar discharge processes for $Fe_2P_2S_6$ and $Ni_2P_2S_6$ electrodes can be assumed based on the XRD investigations.

The pair distribution function (PDF, Figure 4a) obtained from total scattering experiments confirm the loss of crystallinity during Na uptake. PDF analysis demonstrates that long-range order is lost after the uptake of 5 Na/f.u., which is in agreement with results obtained from XRD investigations. At this point, the spatial expansion of the sample only amounts to ~7 Å. While the intensities of the observed distances >7 Å continuously decrease from the pristine material until uptake of 5 Na/f.u., the signals observed at <7 Å show more alterations. While the characteristic distances of $Fe_2P_2S_6$ (*e.g.* 2.04 Å: P–S; 2.55 Å: Fe–S; 3.33 Å: P–S; 3.43 Å: Fe–Fe; 3.59 Å: Fe–P; 3.75 Å: P–S; 4.27 Å: Fe–S; 5.49 Å: Fe–S; 5.89/5.92 Å: P–S; 5.93 Å: Fe–S; 5.95 Å: Fe–Fe/P–P/S–S) steadily decrease until 3 Na/f.u., some new signals (2.33 Å, 2.79 Å and 3.81 Å) develop and increase until ~5 Na/f.u. After uptake of 5 Na/f.u., the intensities of the signals at 2.33 and 3.81 Å decrease again, while the intensity of the signal at 2.79 Å further increases. Finally, the most intense distances are observed at 2.37 and 2.79 Å in the discharged state. Although the intensity beyond 7 Å has increased slightly, no clear long-range order appears. Instead, distances within medium-range order (~40–50 Å) have developed (see ESI, Figure S5a). Therefore and due to the high probability of the formation of several phases during the discharge process, it is not possible to determine the exact composition of the discharged sample from PDF analysis. Nonetheless, some suggestions can be derived (Figure 4b): i) the most pronounced signals at 2.33 Å and 2.79 Å after uptake of 4–5 Na/f.u. are potentially related to the appearance of elemental Fe (2.50/2.89 Å: Fe–Fe); ii) in the completely discharged state, the intensity ratio of these signals (~2.37 Å and ~2.79 Å) has inverted and the signals match characteristic distances of Na_2S (2.83 Å: Na–S; 3.27 Å: Na–Na), bcc-Fe (2.48/2.87 Å: Fe–Fe) and NaF (2.32 Å: Na–F; 3.28 Å: Na–Na). Besides the possible constituents of the electrodes in different states of discharge, the PDF measurements clearly demonstrate that the active material loses its structural integrity during discharging.

While clear indications of Na_2S formation can be found in the completely discharged electrode (Figure S5b), the assignment of other phases is difficult due to the apparent disordered nature and short- to medium-range order of the samples. Additionally, the presence of several phases results in potential overlapping of signals in the PDF curves, further hampering the assignment. For this reason, PDF analysis does not provide sufficient evidence to predict the exact composition of the examined electrodes. Thus, additional XAS experiments at the Fe K-edge as well as ^{23}Na and ^{31}P MAS NMR measurements were conducted to gather further insights into the reaction mechanism.

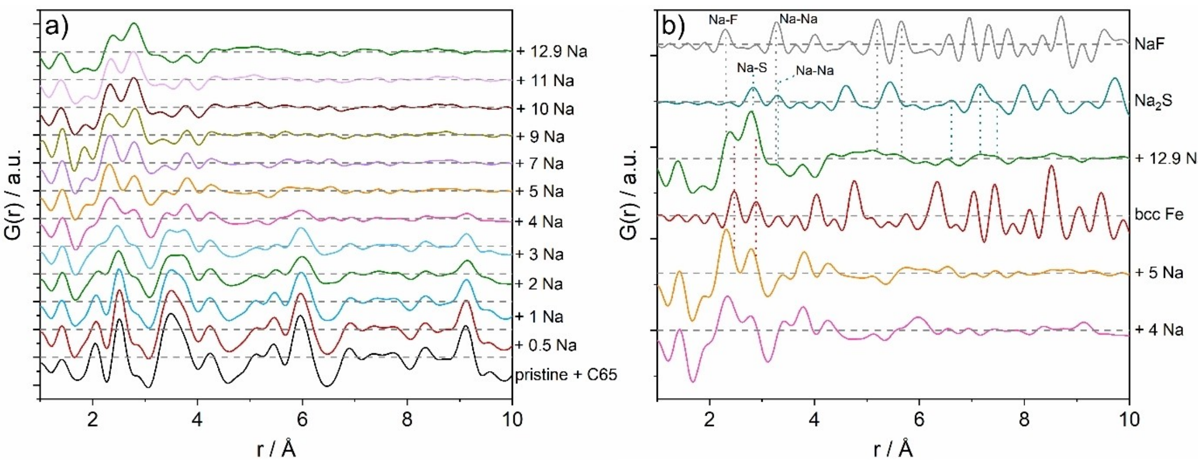

Figure 4. Pair distribution function (PDF) of $Fe_2P_2S_6$ electrodes after uptake of distinct amounts of Na/f.u. (a) PDF in the range between 1.0 and 10 Å. PDFs of pristine $Fe_2P_2S_6$ mixed with carbon as well as electrodes after the uptake of 0.5–12.9 Na/f.u. are shown. (b) PDF in the range of 1–10 Å showing the electrodes after uptake of 4 and 5 Na/f.u. as well as in the discharged state (12.9 Na/f.u.) and PDF calculated from literature data of Na_2S,[40] bcc-Fe[41] and NaF.[42]

X-Ray Absorption Experiments

X-ray absorption near-edge spectra (XANES) collected at the Fe K-edge (Figure 5a) enabled further insights into the ongoing reaction during the discharge process. The Fe K-edge energy of the pristine $Fe_2P_2S_6$ is 7119.5 eV (Figure 5b; 1st derivatives), while a very weak pre-edge feature (quadrupole allowed 1 s→3d transition) is present at an energy of ~7111.7 eV, which is in agreement with octahedral environment of Fe^{2+} cations in the structure. The white line (1 s→4p transition) occurs at ~7125 eV. During sodium uptake, the intensity of the Fe K-edge steadily decreases, and the intensity of the pre-edge increases and slightly shifts to 7111.9 eV, while the spectra rotate around an isosbestic point located at ~7119 eV. Furthermore, the white line at 7125 eV completely vanished during discharging and the Fe K-edge energy of the completely discharged sample matches that of the Fe reference. It is noteworthy that most of the characteristic XANES features disappeared entirely and that the Fe K-edge is less pronounced in the spectrum of the discharged sample compared to the Fe reference. The differences between the spectra of the discharged sample and the Fe reference arise from the differences in crystallinity and particle size. While the Fe reference is a highly crystalline bcc-Fe foil, the Fe generated during discharging is highly disordered and consists of nanoparticles, which exhibit a large number of defects on the surface and a higher ratio of surface to volume atoms as well. Additionally, the observed blurry and unpronounced appearance of the spectrum is a well-known phenomenon for metal nanoparticles and amorphous alloys.[24,25,30,43,44]

Similar to $Ni_2P_2S_6$, the biggest changes in the spectra occur up to the uptake of ~5 Na/f.u., and only minor alterations (slightly increasing Fe K-edge and decreasing white line intensity) are detected upon further Na uptake. Thus, the majority of Fe^{2+} is reduced to Fe^0 after uptake of ~5 Na/f.u., while the rotation around an isosbestic point (~7119 eV) suggests that no intermediary steps occur during the reduction of Fe^{2+}. Summarizing, the XANES experiments show that the occurring reactions of $Fe_2P_2S_6$ and $Ni_2P_2S_6$ electrodes during discharging closely resemble each other (*cf.* ref. [24]).

In addition, XAS data were used to obtain pseudo-radial distribution functions (pRDF) through Fourier-transformation of the EXAFS region (Figure 6). The pRDF of pristine $Fe_2P_2S_6$ exhibits two signals at 2.01 and 3.11 Å (note: data were not phase-shift corrected), representing the Fe–S (2.54 Å), Fe–Fe (~3.43 Å) and Fe–P (~3.60 Å) distances, respectively. The pRDF clearly reveals that $Fe_2P_2S_6$ decomposes during the discharge process. The signal of the pristine sample at 2.01 Å is split into two signals (1.82 and 2.32 Å) of lower intensity after the uptake of 2.5 Na/f.u. While the signal at 1.82 Å gains intensity upon further Na uptake, the intensity of the other signal decreases. At 5 Na/f.u., only a single signal at ~1.9 Å is present and further Na uptake does not lead to significant alterations. The first signal of the Fe reference occurs at 2.22 Å in the pRDF. As already discussed, the differences between the discharged sample and the Fe foil is caused by the highly defective and nanoscopic nature of the particles in the discharged sample compared to the perfect bcc-Fe. The EXAFS data confirms that the reduction of Fe^{2+} largely takes place up to 5 Na/f.u., as already suggested by the XANES spectra, and further indicates that the discharge mechanism of $Fe_2P_2S_6$ and $Ni_2P_2S_6$ correspond to each other (*cf.* ref. [24]).

Magic-Angle-Spinning Nuclear Magnetic Resonance Experiments of the ^{23}Na and ^{31}P Nuclei

While XRD and XAS experiments presented strong evidence for the formation of Na_2S and elemental Fe, the formation of an amorphous intermediate phase is indicated but its composition is not unraveled conclusively. Therefore, ^{31}P and ^{23}Na MAS NMR experiments (Figure 7) were conducted to address the unknown amorphous phases appearing during the discharge reaction. It

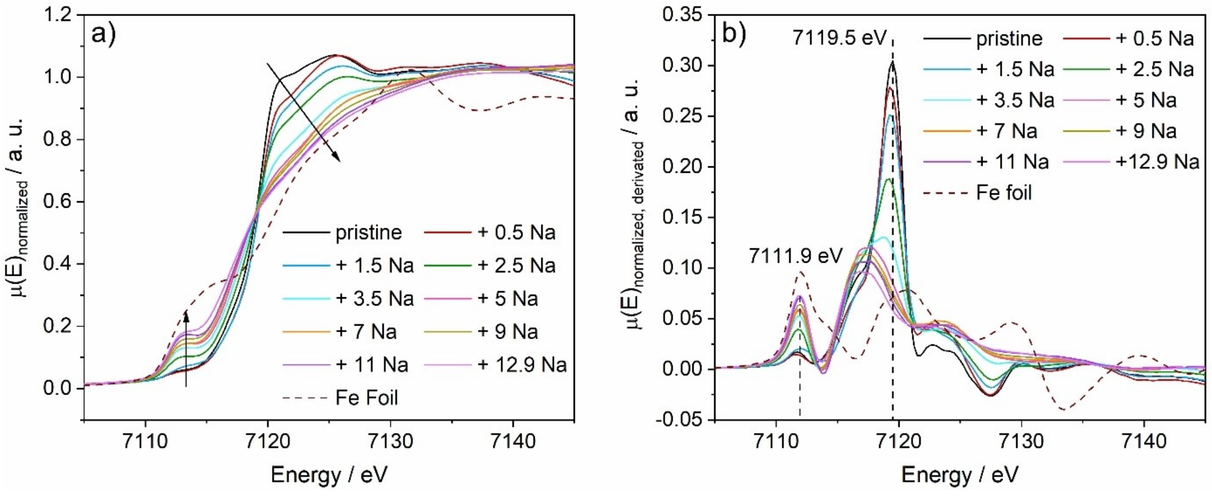

Figure 5. X-ray absorption spectra (XAS) of $Fe_2P_2S_6$ electrodes and of different discharge states. (a) X-ray near edge spectra (XANES) of several samples within the discharge process and (b) the corresponding 1st derivatives of the spectra.

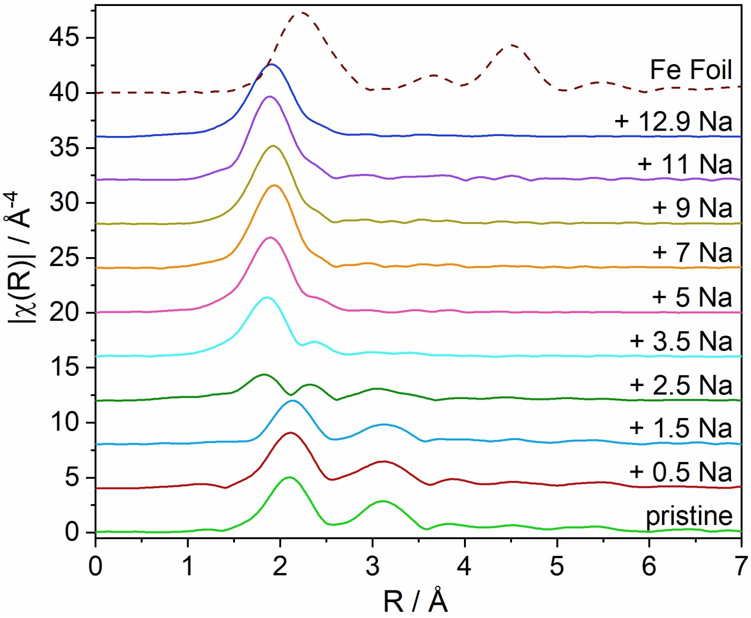

Figure 6. FT radial distances for Fe absorber atoms of the pristine $Fe_2P_2S_6$ electrode and of different discharge states.

is noteworthy that the ^{31}P MAS NMR spectrum (Figure 7a) of $Fe_2P_2S_6$ does not show any signals, which is surprising because a clear and well-resolved signal was observed for the similar compound $Ni_2P_2S_6$ exhibiting a chemical shift of −474 ppm.[24] Although the absence of this signal was not expected here, a similar behavior has been observed for $CrPS_4$.[25] Nevertheless, a broad signal with a chemical shift of 107 ppm, which exhibits a shoulder ranging from ~80 to ~7 ppm, emerged during the discharge process. While this signal reaches maximum intensity after the uptake of 5 Na/f.u., early signs of its formation (i.e. slightly enhanced intensity) are detectable already after the insertion of 2.5–3.5 Na/f.u. This signal strongly corresponds to the chemical shifts of the reference material $Na_4P_2S_6\cdot 6H_2O$ of 101 ppm. We note that the formation of the dehydrated compound $Na_4P_2S_6$ is more likely. However, these two compounds exhibit roughly the same chemical shifts (113 ppm[45] (dehydrated) vs. 101 ppm (hydrated) for the main resonance) due to a very similar local environment of phosphorus atoms in these compounds. Furthermore, the Li analogue $Li_4P_2S_6$ shows a similar chemical shift of 108–110 ppm[46] for the $[P_2S_6]^{4-}$ anion. Consequently, the signal of the $Fe_2P_2S_6$ electrode after the uptake of 5 Na/f.u. is ascribed to the formation of $Na_4P_2S_6$ as the amorphous intermediate. Further discharging beyond 5 Na/f.u. leads to steadily decreasing intensity and broadening of these signals. In the completely discharged state, the signal almost vanished completely and the most intense signal in this state is located at a chemical shift of 7 ppm. The area of slightly increased intensity (400–40 ppm) next to the small signal at 7 ppm is vaguely reminiscent of the ^{31}P MAS NMR signal of red phosphorus (see ESI Figure S6 for a more detailed view), which might be a sign of a local structure resembling some structural motifs related to P_n polymers. We further note that no signs of phosphide formation have been observed and that the broad nature of the observed signals is a consequence of the presence of magnetic Fe nanoparticles.

The ^{23}Na NMR spectrum of $Fe_2P_2S_6$ (Figure 7b) displays only the baseline, which is expected in this case. Discharging leads to the emergence of a signal as early as the uptake of 1.5 Na/f.u., which initially appears as very broad signal with low intensity and eventually reaching its maximum after the uptake of 5 Na/f.u. exhibiting a chemical shift of around -25 ppm. However, this broad signal ranges from a chemical shift of 25 to −80 ppm and resembles the ^{23}Na MAS NMR spectrum of the $Na_4P_2S_6\cdot 6H_2O$ reference (chemical shift: −24 ppm), strengthening the hypothesis that $Na_4P_2S_6$ is generated as amorphous intermediate during discharging. Further Na uptake first results in decreasing intensity (up to 9 Na/f.u.) and subsequently leads to a narrowing and again slightly increasing intensity of this signal in the discharged state. Moreover, a new signal emerges at 37.4 ppm after the uptake of 9 Na/f.u., which gains intensity until the electrode is completely discharged. This signal is clearly associated with Na_2S formation and therefore confirms the results obtained from XRD experiments and corresponds to observations made for $Ni_2P_2S_6$ electrodes (*cf.* ref. [24]). The second NMR resonance in the discharged state with a chemical shift of −25 ppm can be explained by SEI components, such as NaF, which is a common observation for certain electrolyte salts.[24–28,30]

It is noteworthy that the NMR spectra presented here do not exhibit a very good resolution and some NMR resonances are slightly shifted. This is largely because the samples that were examined here are not ideally suited for such experiments, primarily because they contain ferromagnetic Fe nanoparticles and the induced local magnetic fields at these particles potentially influence the resolution and chemical shift of the NMR resonances. Nonetheless, the NMR studies reveal close

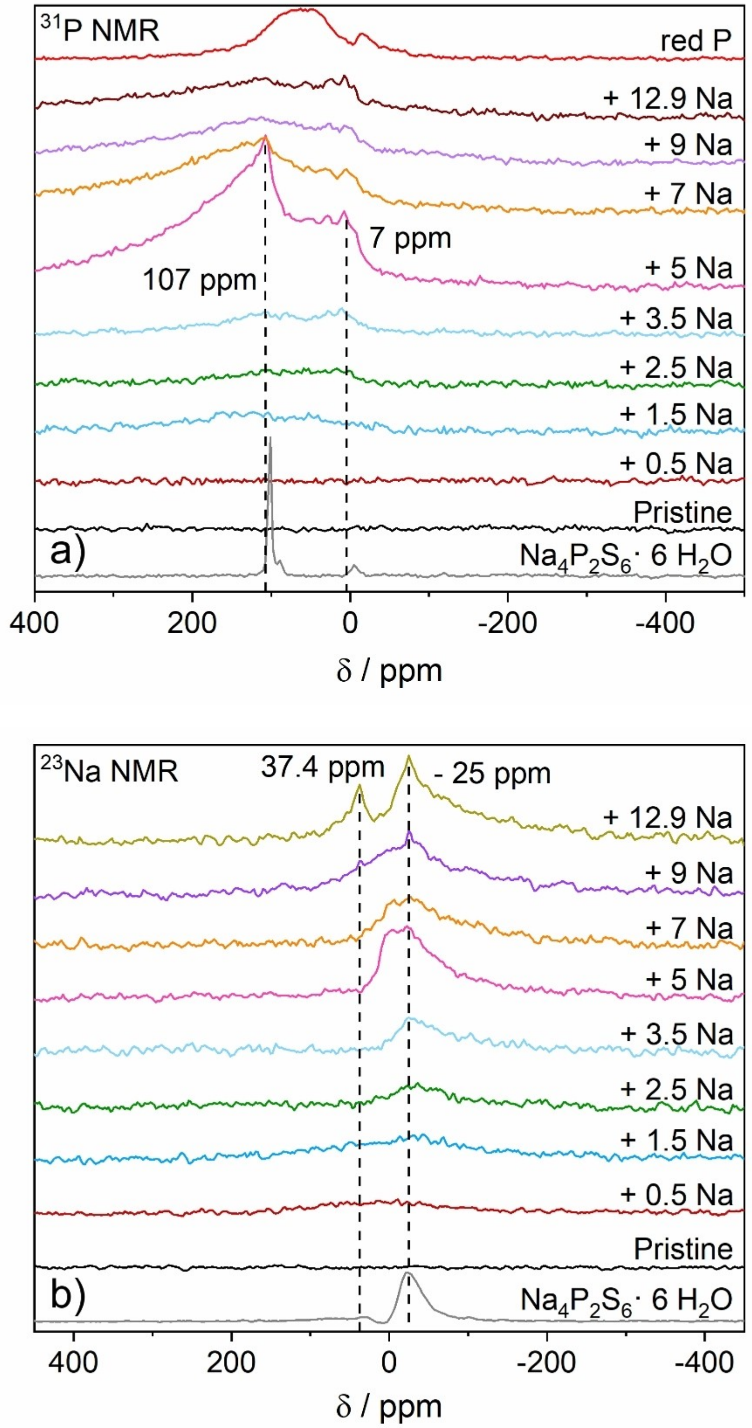

Figure 7. (a) ^{31}P NMR and (b) ^{23}Na MAS NMR spectra of $Fe_2P_2S_6$ electrodes with different amounts of Na inserted into the electrode during the discharge process.

resemblance between the sodium uptake mechanism of $Fe_2P_2S_6$ and $Ni_2P_2S_6$ electrodes.

Shortly summarizing, the MAS NMR experiments indicate that the occurring reaction induced by sodium uptake is very similar for $Fe_2P_2S_6$ and $Ni_2P_2S_6$. Especially the identification of $Na_4P_2S_6$ as intermediate phase points towards an analogous reaction pathway.

Conclusion

In this study, we focused on the electrochemical behavior and the ongoing reaction mechanism of $Fe_2P_2S_6$ in SIBs. The findings concomitantly were utilized to compare the behavior of $Fe_2P_2S_6$ electrodes with previously investigated anode material $Ni_2P_2S_6$. $Fe_2P_2S_6$ was synthesized successfully by a chemical vapor transport approach. Phase purity was demonstrated by XRD and combined EDX and elemental analysis. Galvanostatic experiments revealed long-term stability with reversible capacities around 540 $mAh\,g^{-1}$ in the 250th and 614 $mAh\,g^{-1}$ in the 190th cycle (compared to 621 $mAh\,g^{-1}$ in 190th cycle for $Ni_2P_2S_6$), clearly showing equally good electrochemical properties for $Fe_2P_2S_6$ and $Ni_2P_2S_6$. Moreover, these two materials exhibit similar rate capabilities. However, $Fe_2P_2S_6$ is slightly less tolerant against high currents ($\geq 2.0\ A\,g^{-1}$), while on the other side, it exhibits minor advantages in capacity retention when switching back to low currents (here: from 3.0 to 0.2 $A\,g^{-1}$). The changes of specific capacity during extended periods of cycling are caused by a steady change of the underlying reaction mechanism for either of the two compounds. Based on the electrochemical experiments, the XRD and PDF investigations, the analysis of the NMR spectra and of the XANES curves, the reaction can be summarized as follows: i) at the beginning Na is intercalated into the van der Waals gaps of $Fe_2P_2S_6$; ii) further Na uptake reduces the crystallinity of $Fe_2P_2S_6$ until 4–5 Na/f.u. is reached; iii) at this stage, an amorphous intermediate is formed and Fe^{2+} is reduced to elemental nanoscopic Fe; iv) the intermediate is most probably $Na_4P_2S_6$; v) at the end of discharging, nanocrystalline Na_2S and a polymeric phosphorus species are generated.

At this point, we want to note that $Fe_2P_2S_6$ behaves very similar to $Ni_2P_2S_6$. Therefore, we propose the following general reaction mechanism for $M_2P_2S_6$ (M=Ni, Fe):

$$M_2P_2S_6 \xrightarrow{+4\ Na} 2M^0 + Na_4P_2S_6 \xrightarrow{+8\ Na} 2M^0 + Na_2S + \frac{2}{n}P_n \qquad (5)$$

In Eq. (5), we propose a reaction mechanism involving uptake of 12 Na/f.u., although electrochemically ~13 Na/f.u. were inserted into the $Fe_2P_2S_6$ electrode. The difference of 1 Na/f.u. is assigned to SEI formation and potentially to some extent co-intercalation. While this uptake of an extra 1 Na/f.u. obviously might as well result in the formation of a Na_xP phase, no signs of such compounds were found, but PDF and ^{23}Na MAS NMR experiments indicate NaF formation, which is a common component of the SEI. Conversely, $Ni_2P_2S_6$ electrodes take up 12.1 Na/f.u. and only few signs of SEI compounds are found in the discharged state.[24] This is an indication for the formation of a thinner SEI in $Ni_2P_2S_6$ electrodes, potentially being responsible for the small differences in the electrochemical behavior of the two materials and further indicating that uptake of >12 Na/f.u. probably can be ascribed to SEI generation in either case.

Experimental Section

Synthesis

$Fe_2P_2S_6$ was synthesized via chemical vapor transport from stoichiometric amounts of elemental iron (Alfa Aesar, 99.9%), red phosphorus (Knapsack AG, 99.9999%) and an excess of sulfur (Chempur, 99.999%). The mixture was filled in a quartz tube, which then was evacuated ($<10^{-4}$ mbar) and sealed. The reaction vessel was heated in a tube furnace within 4 h to 723 K and the temperature was maintained for 24 h. Thereafter, the temperature was increased to 923 K within 2 h and this temperature was held for 2 weeks. After the furnace had reached the target temperature of 923 K, a temperature gradient to 908 K was established to initiate the vapor transport.

Electrochemical Tests

Working electrodes were prepared by mixing the active material $Fe_2P_2S_6$ with SUPER C65 (Timcal, Switzerland) and polyvinylidene difluoride (PVDF, Solvay, Germany) in a ratio of 70:20:10 wt%, suspending the mixture in *N*-methyl-2-pyrrolidone (NMP, Fisher Bioreagens, 99.8%) and spreading the suspension on Cu foil via doctor-blade method. The wet electrode film was dried over night at room temperature. Afterwards, the electrode was put in a vacuum oven at 333 K and further dried for several hours. The dry electrode film was punched into circular electrodes with a diameter of 10 mm (0.63–0.91 mg active material) and assembled in Swagelok-type cells. The assembly was conducted inside a glovebox filled with argon (99.999% Ar, MBraun Unilab; <1 ppm O_2; <1 ppm H_2O). The $Fe_2P_2S_6$ electrode was tested as working electrode against sodium metal as counter electrode. A glass fibre filter (Whatman™, United Kingdom) and a Celgard® membrane were used as separators and a solution of 1 M $NaCF_3SO_3$ (abcr, 98%) in bis(2-methoxyethyl)ether (Diglyme, Acros Organics, 99+%, extra dry) was utilized as electrolyte.

Galvanostatic long-term stability and rate capability measurements were performed within a potential range of 3.0–0.1 V using MTI or Neware 8 channel battery analyzer and applying a current rate of 1 $A\,g^{-1}$ for stability tests and rates between 0.2 and 3.0 $A\,g^{-1}$ for rate capability experiments. A constant current – constant voltage (CCCV) charge mode with a cutoff current of one-fifth of the initial rate was applied for all galvanostatic measurements with current rates $\geq 1.0\ A\,g^{-1}$.

Material Characterizations

X-ray diffraction (XRD) patterns were collected on a PANalytical diffractometer equipped with a 1D PIXcel detector and an X-ray tube generating Cu-K_α radiation ($\lambda = 1.54058$ Å). Elemental (CHNS) analysis was performed with a Vario MICRO cube elemental analyzer (Elementar) and using sulphanilamide as a standard material. EDX spectra and SEM images were collected using a Philips ESEM XL 30 system, equipped with an EDAX New XL-30 detector.

Investigation of the Reaction Mechanism

For investigations of the reaction mechanism, a mixture of 70 wt% $Fe_2P_2S_6$ and 30 wt% SUPER C65 was pressed into pellets and assembled in Swagelok-type cells as described before. After uptake of a certain amount of Na, the electrochemical reaction was stopped, and the cells were transferred into an argon-filled glovebox, disassembled and the samples were rinsed with pure diglyme to remove residual electrolyte from the surface of the electrodes. The electrodes were dried for 1 day in the glovebox. These samples were handled permanently in inert atmosphere.

The samples were prepared in borosilicate capillaries with a diameter of 0.7 mm for XRD and PDF experiments. These experiments were conducted in Debye-Scherrer geometry with high-energy synchrotron radiation (60 keV) at beamline P02.1, PETRA III (DESY, Hamburg) at a wavelength of $\lambda = 0.207$ Å. The sample detector distance (SDD) for XRD experiments was set to ~1000 mm and for PDF experiments to ~300 mm. The detector was a PerkinElmer XRD1621 2D detector. The obtained 2D data was processed with the program DAWN Science[47] and the software xPDFsuite[48] was utilized to convert the total scattering data to the pair distribution function ($Q_{max} = 19$ Å^{-1}). LaB_6 (NIST 660b) was measured as a standard material to account for instrumental contributions to the XRD and PDF data. Furthermore, an empty borosilicate glass capillary was measured under identical conditions to account for and subtract the contribution of the capillary from the PDF.

For XAS experiments the pellet electrodes were crushed, diluted and mixed with carbon, pressed again into pellets with a diameter of 8 mm and sealed between Kapton foil. The XAS experiments on the Fe K-edge were carried out at the beamline B18, Diamond Light Source (UK). Every spectrum was collected with a data collection time of 3 min. For each sample three spectra were measured, which were merged afterwards. Fe foil was used for energy calibration of the raw data. For background subtraction and normalization, the pre-edge was described using a linear polynomial fit, while for the post-edge region a cubic polynomial fit was used. A calculated background from the built-in Autobk algorithm of the program Athena[49] was utilized for the EXAFS data reduction process. Afterwards, k^3 weighting was applied and an appropriate k-range of 3.2 and 12 Å^{-1} was chosen for the Fourier transformation to obtain a pseudo-radial distribution function (pRDF) $|\chi(R)|$. The k^3-weighted function $\chi(k)$ was multiplied by a Kaiser-Bessel window prior to Fourier transformation. The obtained distances of the pRDF were not phase-shift corrected.

^{23}Na and ^{31}P magic-angle spinning (MAS) nuclear magnetic resonance (NMR) spectroscopy was carried out with a Bruker Avance 200 MHz spectrometer at a magnetic field of 4.7 T, which corresponds to Larmor frequencies of 52.9 MHz (^{23}Na) and 81.0 MHz (^{31}P). Spinning of the samples was conducted in rotors with a diameter of 1.3 mm at a spinning frequency of 50 kHz. To avoid dead time effects during data acquisition, a rotor-synchronized Hahn-echo pulse sequence ($\pi/2$-τ-π-τ-acq.) was applied. The $\pi/2$ pulse lengths were 1.4 μs (^{23}Na) and 0.9 μs (^{31}P) with a recycle delay of 1 s in both cases. The spectra were referenced to 1 M NaCl at 0 ppm (^{23}Na) and to H_3PO_4 (85 %) at 0 ppm (^{31}P).

Supporting Information

Results of EDX and elemental analysis; SEM images; additional discharge and charge (D/C) profiles at elevated cycle numbers; information about pressed powder vs. film electrodes and corresponding D/C profiles and XRD pattern; supporting PDF and ^{31}P MAS NMR data of the discharged state of the electrode

Acknowledgements

Financial support by the State of Schleswig-Holstein is gratefully acknowledged. The authors acknowledge DESY (Hamburg, Germany), a member of the Helmholtz Association HGF, for the provision of experimental facilities. Parts of this research were carried out at PETRA III, beamline P02.1 (proposal BAG-20170560). We kindly thank Huayna Terraschke for beamtime allocation. This work was carried out with the support of the Diamond Light Source, instrument B18 (proposal SP20060). Open Access funding enabled and organized by Projekt DEAL.

Conflicts of interest

The authors declare no conflict of interest.

Data Availability Statement

The data that support the findings of this study are available from the corresponding author upon reasonable request.

Keywords: electrochemistry · $Fe_2P_2S_6$ · reaction mechanism · sodium-ion battery · sodium uptake

[1] M. D. Slater, D. Kim, E. Lee, C. S. Johnson, *Adv. Funct. Mater.* **2013**, *23*, 947–958.
[2] N. Yabuuchi, K. Kubota, M. Dahbi, S. Komaba, *Chem. Rev.* **2014**, *114*, 11636–11682.
[3] W. Luo, F. Shen, C. Bommier, H. Zhu, X. Ji, L. Hu, *Acc. Chem. Res.* **2016**, *49*, 231–240.
[4] J.-Y. Hwang, S.-T. Myung, Y.-K. Sun, *Chem. Soc. Rev.* **2017**, *46*, 3529–3614.
[5] P. K. Nayak, L. Yang, W. Brehm, P. Adelhelm, *Angew. Chem. Int. Ed.* **2018**, *57*, 102–120; *Angew. Chem.* **2018**, *130*, 106–126.
[6] J. Deng, W.-B. Luo, S.-L. Chou, H.-K. Liu, S.-X. Dou, *Adv. Energy Mater.* **2018**, *8*, 1701428.
[7] V. Palomares, P. Serras, I. Villaluenga, K. B. Hueso, J. Carretero-González, T. Rojo, *Energy Environ. Sci.* **2012**, *5*, 5884–5901.
[8] D. Kundu, E. Talaie, V. Duffort, L. F. Nazar, *Angew. Chem. Int. Ed.* **2015**, *54*, 3431–3448; *Angew. Chem.* **2015**, *127*, 3495–3513.
[9] D. Buchholz, A. Moretti, R. Kloepsch, S. Nowak, V. Siozios, M. Winter, S. Passerini, *Chem. Mater.* **2013**, *25*, 142–148.
[10] E. de la Llave, V. Borgel, K.-J. Park, J.-Y. Hwang, Y.-K. Sun, P. Hartmann, F.-F. Chesneau, D. Aurbach, *ACS Appl. Mater. Interfaces* **2016**, *8*, 1867–1875.
[11] D. A. Stevens, J. R. Dahn, *J. Electrochem. Soc.* **2001**, *148*, A803–A811.
[12] D.-Y. Kim, D.-H. Kim, S.-H. Kim, E.-K. Lee, S.-K. Park, J.-W. Lee, Y.-S. Yun, S.-Y. Choi, J. Kang, *Nanomaterials* **2019**, *9*, 793.
[13] B. Xiao, T. Rojo, X. Li, *ChemSusChem* **2019**, *12*, 133–144.
[14] I. El Moctar, Q. Ni, Y. Bai, F. Wu, C. Wu, *Funct. Mater. Lett.* **2018**, *11*, 1830003.
[15] Y. Xiao, S. H. Lee, Y.-K. Sun, *Adv. Energy Mater.* **2017**, *7*, 1601329.
[16] W. Kang, Y. Wang, J. Xu, *J. Mater. Chem. A* **2017**, *5*, 7667–7690.
[17] Z. Hu, Q. Liu, S.-L. Chou, S.-X. Dou, *Adv. Mater.* **2017**, *29*, 1700606.
[18] X. Y. Yu, X. W. (David) Lou, *Adv. Energy Mater.* **2018**, *8*, 1701592.

[19] J. Mao, T. Zhou, Y. Zheng, H. Gao, H. kun Liu, Z. Guo, *J. Mater. Chem. A* **2018**, *6*, 3284–3303.
[20] M. Lao, Y. Zhang, W. Luo, Q. Yan, W. Sun, S. X. Dou, *Adv. Mater.* **2017**, *29*, 1700622.
[21] L. Li, Y. Zheng, S. Zhang, J. Yang, Z. Shao, Z. Guo, *Energy Environ. Sci.* **2018**, *11*, 2310–2340.
[22] T. Wang, D. Su, D. Shanmukaraj, T. Rojo, M. Armand, G. Wang, *Electrochem. Energy Rev.* **2018**, *1*, 200–237.
[23] Y. Liu, W. Li, Y. Xia, *Electrochem. Energy Rev.* **2021**, *4*, 447–472.
[24] J. van Dinter, K. Synnatschke, T. A. Engesser, S. Indris, N. Wolff, O. Gronenberg, M. Etter, G. Cibin, L. Kienle, C. Backes, W. Bensch, *J. Mater. Chem. A* **2020**, *8*, 22401–22415.
[25] J. van Dinter, S. Indris, A. Bitter, D. Grantz, G. Cibin, M. Etter, W. Bensch, *ACS Appl. Mater. Interfaces* **2021**, *13*, 54936–54950.
[26] J. van Dinter, D. Grantz, A. Bitter, W. Bensch, *ChemElectroChem* **2022**, *9*, e202200018.
[27] F. Hartmann, M. Etter, G. Cibin, L. Liers, H. Terraschke, W. Bensch, *Adv. Mater.* **2021**, *33*, 2101576.
[28] S. Senkale, S. Indris, M. Etter, W. Bensch, *ACS Appl. Mater. Interfaces* **2021**, *13*, 26034–26045.
[29] S. Senkale, G. Cibin, A. V. Chadwick, W. Bensch, *ACS Appl. Mater. Interfaces* **2021**, *13*, 58552–58565.
[30] F. Hartmann, M. Etter, G. Cibin, H. Groß, L. Kienle, W. Bensch, *Nanoscale* **2022**, *14*, 2696–2710.
[31] G. Ouvrard, R. Brec, J. Rouxel, *Mater. Res. Bull.* **1985**, *20*, 1181–1189.
[32] A. R. Wildes, V. Simonet, E. Ressouche, G. J. McIntyre, M. Avdeev, E. Suard, S. A. J. Kimber, D. Lançon, G. Pepe, B. Moubaraki, T. J. Hicks, *Phys. Rev. B* **2015**, *92*, 224408.
[33] C. Murayama, M. Okabe, D. Urushihara, T. Asaka, K. Fukuda, M. Isobe, K. Yamamoto, Y. Matsushita, *J. Appl. Phys.* **2016**, *120*, 142114.
[34] A. R. Wildes, V. Simonet, E. Ressouche, R. Ballou, G. J. McIntyre, *J. Phys. Condens. Matter* **2017**, *29*, 455801.
[35] P. Fragnaud, E. Prouzet, R. Brec, *J. Mater. Res.* **1992**, *7*, 1839–1846.
[36] Z. Yang, T. Chen, C. Wu, J. Qu, Z. Wu, X. Guo, B. Zhong, H. Liu, S. Dou, *ACS Appl. Mater. Interfaces* **2019**, *11*, 3961–3970.
[37] J. Y. Park, S. J. Kim, K. Yim, K. S. Dae, Y. Lee, K. P. Dao, J. S. Park, H. B. Jeong, J. H. Chang, H. K. Seo, C. W. Ahn, J. M. Yuk, *Adv. Sci.* **2019**, *6*, 1900264.
[38] M. Krengel, A.-L. Hansen, M. Kaus, S. Indris, N. Wolff, L. Kienle, D. Westfal, W. Bensch, *ACS Appl. Mater. Interfaces* **2017**, *9*, 21283–21291.
[39] M. Krengel, A.-L. Hansen, F. Hartmann, J. van Dinter, W. Bensch, *Batteries & Supercaps* **2018**, *1*, 176–183.
[40] E. Zintl, A. Harder, B. Dauth, *Z. Elektrochem. Angew. Phys. Chem.* **1934**, *40*, 588–593.
[41] E. A. Owen, E. L. Yates, *Philos. Mag.* **1933**, *15*, 472–488.
[42] Y. Shirako, Y. G. Shi, A. Aimi, D. Mori, H. Kojitani, K. Yamaura, Y. Inaguma, M. Akaogi, *J. Solid State Chem.* **2012**, *191*, 167–174.
[43] S. Permien, T. Neumann, S. Indris, G. Neubüser, L. Kienle, A. Fiedler, A.-L. Hansen, D. Gianolio, T. Bredow, W. Bensch, *Phys. Chem. Chem. Phys.* **2018**, *20*, 19129–19141.
[44] W. K. Luo, H. W. Sheng, F. M. Alamgir, J. M. Bai, J. H. He, E. Ma, *Phys. Rev. Lett.* **2004**, *92*, 145502.
[45] T. Scholz, C. Schneider, R. Eger, V. Duppel, I. Moudrakovski, A. Schulz, J. Nuss, B. V. Lotsch, *J. Mater. Chem. A* **2021**, *9*, 8692–8703.
[46] C. Dietrich, D. A. Weber, S. Culver, A. Senyshyn, S. J. Sedlmaier, S. Indris, J. Janek, W. G. Zeier, *Inorg. Chem.* **2017**, *56*, 6681–6687.
[47] J. Filik, A. W. Ashton, P. C. Y. Chang, P. A. Chater, S. J. Day, M. Drakopoulos, M. W. Gerring, M. L. Hart, O. V. Magdysyuk, S. Michalik, A. Smith, C. C. Tang, N. J. Terrill, M. T. Wharmby, H. Wilhelm, *J. Appl. Crystallogr.* **2017**, *50*, 959–966.
[48] X. Yang, P. Juhas, C. L. Farrow, S. J. L. Billinge, arXiv:1402.3163 **2014**.
[49] B. Ravel, M. Newville, *J. Synchrotron Radiat.* **2005**, *12*, 537–541.

Manuscript received: June 29, 2022
Revised manuscript received: September 6, 2022
Accepted manuscript online: September 8, 2022